ISSN (Print) 1226-1750
ISSN (Online) 2233-6656
Journal of Magnetics 26(2), 194-198 (2021) https://doi.org/10.4283/JMAG.2021.26.2.194

Phase Distribution and Coercivity Enhancement in (MM,Nd)-Fe-B Magnets with Dual-main-phase

Dong-wei Duan[1,2], Lei Wei[1], Zhu-bai Li[1,2]*, Qian Zhao[1,2], and Yong-feng Li[1,2]

[1]*Key Laboratory of Integrated Exploitation of Bayan Obo Multi-Metal Resources, Inner Mongolia University of Science and Technology, Baotou 014010, China*
[2]*School of Science, Inner Mongolia University of Science and Technology, Baotou 014010, China*

(Received 28 February 2021, Received in final form 17 June 2021, Accepted 18 June 2021)

The mischmetal-based sintered magnets were prepared by mixing $MM_{8.8}Nd_{3.4}Fe_{81.8}B_6$ (MM denotes mischmetal) with $Nd_{15}Fe_{79}B_6$ alloys. The magnet consist of two main phases i.e., (La,Ce)-rich main phase and Nd-rich main phase. For the mass ratio of 8:2 of $MM_{8.8}Nd_{3.4}Fe_{81.8}B_6$ and $Nd_{15}Fe_{79}B_6$, many grains of La-Ce-rich main phase are interconnected and the effect of enhancing the coercivity is weak in the sintered magnets. While for the mass ratio of 6:4 most grains of (La,Ce)-rich main phase are nearly separated and covered by the Nd-rich main phase and intergranular phase, and the coercivity increases significantly to 7.70 kOe. Compared with $(MM_{0.3}Nd_{0.7})_{30.3}Fe_{bal}B_{0.96}Cu_{0.1}Al_{0.11}$ magnets prepared by the conventional method, the coercivity doesn't decrease in the sintered composite magnets of $MM_{8.8}Nd_{3.4}Fe_{81.8}B_6/Nd_{15}Fe_{79}B_6$ though the MM content of 40 wt.% is higher. The optimization of Nd-rich-main-phase distribution as well as Nd substitution for La-Ce should be responsible for the significant increase of coercivity.

Keywords : mischmetal-based magnets, composite magnets, phase distribution, substitution, coercivity

1. Introduction

The composite technology is beneficial to enhance the magnetic properties in the hybrid magnets [1-5]. The mischmetal (MM) is the unseparated rare-earth and contains about 75 wt.% of La-Ce [6, 7], and the coercivity could be improved in the sintered magnets of $MM_2Fe_{14}B$/$Nd_2Fe_{14}B$ [8, 9], though the magnetocrystalline anisotropy is much lower and the coercivity is very weak in $MM_2Fe_{14}B$ [10-12]. This gives a way to utilize La-Ce elements more efficiently for decreasing the consumption of Nd and reducing the purification cost. It is noted that different from that in the nanocomposite magnets the grain size is in micrometer scale in the sintered composite magnets [13, 14]. The underline mechanism of magnetic properties enhancement remains unclear in $MM_2Fe_{14}B$/$Nd_2Fe_{14}B$ magnets with the hybrid structure. It also has received the increasing attention what the phase distribution is and how the microstructure affects the coercivity in the sintered magnets with the grain size in micrometer scale [15]. In this paper, the influences of Nd-Fe-B addition into $MM_{8.8}Nd_{3.4}Fe_{81.8}B_6$ were investigated in the sintered magnets, which is helpful to understand fully the relationship between the phase distribution in microstructure and the coercivity enhancement in the dual-main-phase mischmetal-based magnets.

2. Experimental

$MM_{8.8}Nd_{3.4}Fe_{81.8}B_6$ and $Nd_{15}Fe_{79}B_6$ powders with the averaged size of about 3 μm were prepared, respectively, by the induction melting, hydrogen decrepitation and jet-milling. The mischmetal was purified from Bayan Obo Mine in Baotou of China. The content is same with that in Ref. 5, and the weight percentage of La-Ce is 78.76 %. The two types of powders were mixed according to the mass ratios (MR) of 10:0, 9:1, 8:2, 7:3 and 6:4, respectively, and then aligned and compacted to a green cylinder. The vacuum sintering was performed at the temperatures of 1030 ºC to 1040 ºC for 2 hours and annealed at 510 ºC for 2 hours to optimize the coercivity. X-ray Diffraction (XRD) was carried out to check the phase structure using Co Kα radiation. The scanning electron microscope (SEM) and electron probe microanalyzer (EPMA) were

*Corresponding author: Tel: +86-472-5953508
Fax: +86-472-5953508, e-mail: lzbgj@163.com

used, respectively, to observe the surface topography and the elemental distribution. The magnetic properties were recorded using NIM-200C Loop Tracer at room temperature. The magnetization reversal of thermal activation was recorded using QD Versalab at temperature of 300 K.

3. Results and Discussion

The XRD patterns of the powders are illustrated in Fig. 1, and the pattern of the aligned magnet for mass ratio of 6:4 is also shown in Fig. 1. The diffraction peaks are strong for the crystal planes of (105) and (006), indicating the alignment and anisotropic nature for the mangnts. According to the analysis using Jade software, the main phase is $R_2Fe_{14}B$ phase in these sintered magnets, but there exist the minor phases of the rare-earth-rich oxide, RFe_2 and RFe_4B_4 [16, 17]. The minor phases with paramagnetism at the grain boundary are necessary to decouple the interaction for enhancing the coercivity. The demagnetization curves and the variations of the magnetic properties are shown in Fig. 2(a) and (b), respectively. Even with nearly the same phase constitution, the magnetic properties are much different among these magnets. In $MM_{8.8}Nd_{3.4}Fe_{81.8}B_6$, the coercivity H_c of 2.39 kOe is rather low due to the high content of La-Ce in the magnets. The coercivity increases with the addition of $Nd_{15}Fe_{79}B_6$ powders, and especially for the mass ratio of 6:4 it increases significantly. The addition of $Nd_{15}Fe_{79}B_6$ also gives rise to the improvements in both the remanence B_r and the energy product $(BH)_{max}$. The coercive field of 7.70 kOe were acquired with the maximum energy product of 33.67 MGOe in the magnet of $MM_{8.8}Nd_{3.4}Fe_{81.8}B_6$/$Nd_{15}Fe_{79}B_6$ for the mass ratio of 6:4, and about 40 wt.%

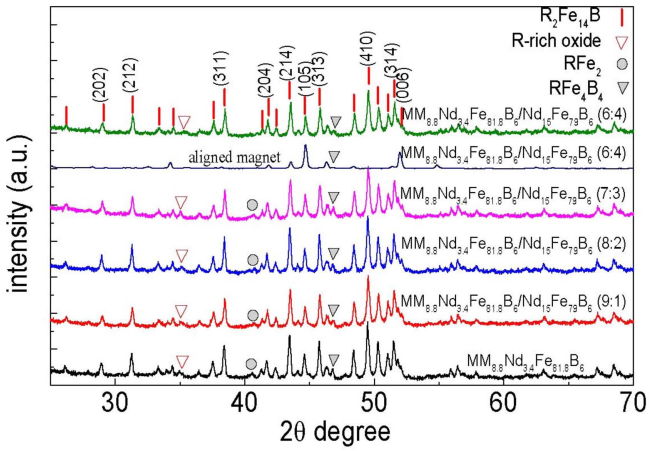

Fig. 1. (Color online) XRD patterns of the sintered magnets measurement by Co Kα radiation for the mass ratios (MR) of 10:0, 9:1, 8:2, 7:3 and 6:4, respectively.

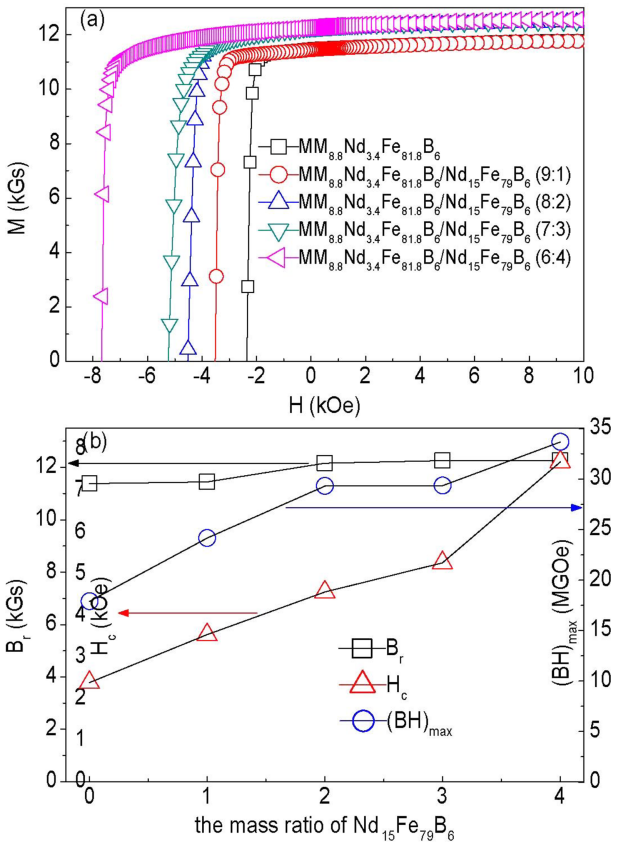

Fig. 2. (Color online) The demagnetization curves (a), and the dependences of remanence, coercive field and energy product (b) on the mass ratio of $Nd_{15}Fe_{79}B_6$ powders.

Nd is substituted by MM. In magnet of $(MM_{0.3}Nd_{0.7})_{30.3}$-$Fe_{bal}B_{0.96}Cu_{0.1}Al_{0.11}$ prepared by the conventional method, the coercivity was 7.60 kOe and the substitution amount of MM was about 30 wt.% [18]. By comparison, in the sintered composite magnets of $MM_{8.8}Nd_{3.4}Fe_{81.8}B_6$/$Nd_{15}Fe_{79}B_6$, the MM substitution amount of 40 wt.% is greater and the coercivity doesn't decrease.

In nanocomposite magnets the coercivity enhancement is attributed to the grain size in nanometer scale and intergranular exchange coupling [19], but in the sintered composite magnets the grain size is in micrometer scale. Fig. 3 displays the SEM images of polished surfaces in the magnets with the mass ratio of 10:0, 8:2 and 6:4. The intergranular rare-earth-rich phases are mainly distributed at the grain triple-junction, and their color is brighter. The color of main phase $R_2Fe_{14}B$ is deeper, and the grain size is almost in the range between 1 and 5 μm. For observing the difference in microstructure among these magnets, the element distributions were investigated and shown in Fig. 4, and left, middle and right are La, Ce and Nd mappings, respectively. The chemical composition could be identified according to the colors of blue, green, yellow and red

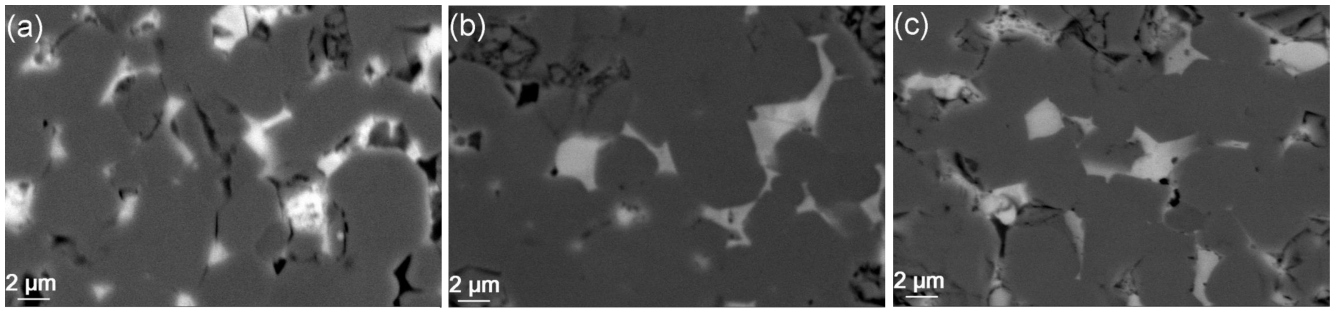

Fig. 3. The surface micromorphology in the sintered magnets for the mass ratios of $MM_{8.8}Nd_{3.4}Fe_{81.8}B_6$ and $Nd_{15}Fe_{79}B_6$ of 10:0 (a), 8:2 (b) and 6:4 (c).

on the right label. The intergranular phase is rich in rare-earth and curved by deep-red circles. The main phases of $R_2Fe_{14}B$ contains lower content of rare-earth, which can be divided into two classes, i.e., (La,Ce)-rich main phase curved by white circles and Nd-rich main phase curved by red circles.

Note that in the grains of the main phase the chemical compositions are not the same. As shown in Ce mapping of Fig. 4(a), in $MM_{8.8}Nd_{3.4}Fe_{81.8}B_6$ magnets without the addition of $Nd_{15}Fe_{79}B_6$ powders there exist the grains of Nd-rich main phase, some of which are indicated by the white arrows. The structure stability of $(La,Ce)_2Fe_{14}B$ crystal is different from that of $Nd_2Fe_{14}B$ [20, 21]. La and Ce are more probably expelled from the $R_2Fe_{14}B$ crystal, while Nd atoms are more easily enter into $R_2Fe_{14}B$ crystal and replace La-Ce due to the different diffusion thermodynamics for La, Ce and Nd [18]. Bearing this in mind, it is reasonable to infer that the anisotropy is improved in (La,Ce)-rich main phase owing to the entrance and substitution of Nd atoms [22, 23].

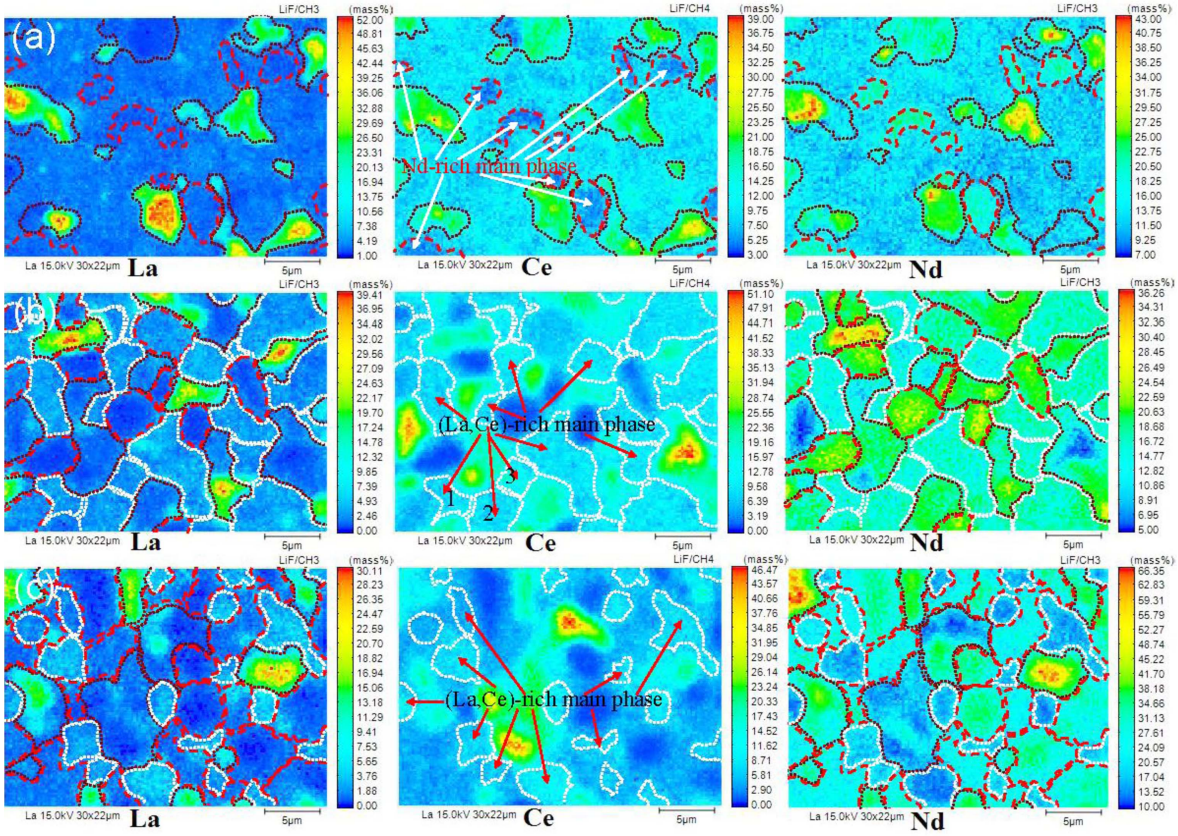

Fig. 4. (Color online) The elemental distributions of La, Ce and Nd in the sintered magnets with the mass ratios of 10:0 (a), 8:2 (b) and 6:4 (c).

The addition of $Nd_{15}Fe_{79}B_6$ powders results in the increase in the region area of Nd-rich main phase. For the mass ratio of 8:2, many grains of La-Ce-rich main phase, e.g., the grains marked 1, 2, and 3 are interconnected in the sintered composite magnets (shown in Ce mapping of Fig. 4(b)). While for the mass ratio of 6:4, the grains of (La,Ce)-rich main phase are nearly separated and covered by the Nd-rich main phase and intergranular phase, and this high coverage and optimization of Nd-rich main phase distribution may be the main reason why the coercivity increases significantly.

For checking the magnetization reversal and the origin of coercivity enhancement, the thermal activation and the aftereffect were investigated, since thermal activation is the nonreversible magnetization reversal by passing over an activation volume due to thermal fluctuation [24]. As illustrated in Fig. 5, on the sample magnetized to the saturation state, a negative field was applied close to the coercive field and held for 1200 sec, followed by a rise at the rate of 10 Oe/sec. The aftereffect field of thermal activation, acquired via fitting the tangents of magnetization curve to the point of intersection, is actually the fluctuation field H_f [25]. The activation sizes d_{active} is related to the fluctuation field. According to the equations of $dactive = \sqrt[3]{v}$ and $v = k_B T/H_f M_s$ (v is the activation volume, $k_B = 1.38 \times 10^{-23}$ J/K, $T = 300$ K, and $M_s = 1.4$ T) [26, 27], the obtained activation sizes are several nanometers (shown in the inset of Fig. 5), nearly the same with the theoretical domain wall size δ_m of $R_2Fe_{14}B$ magnets [24]. It suggests that the domain wall nucleation is undergone in low anisotropy phase of (La,Ce)-rich main phase in the magnetization reversal of thermal activation [25].

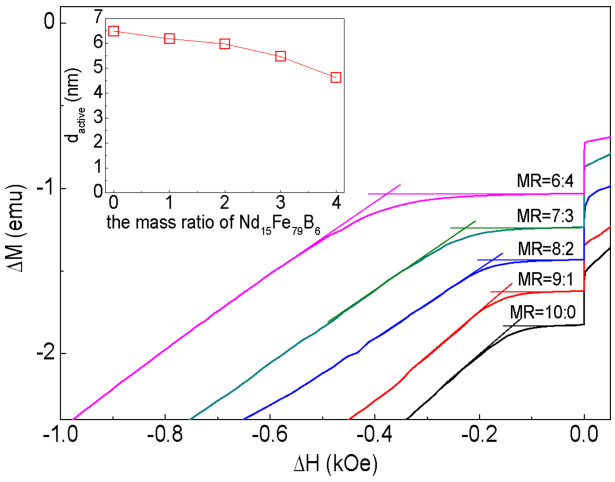

Fig. 5. (Color online) The demagnetization curves for rising the field at a rate of 10 Oe/sec following the magnetization reversal of thermal activation, and the inset shows the dependence of activation size d_{active} on the mass ratio of $Nd_{15}Fe_{79}B_6$.

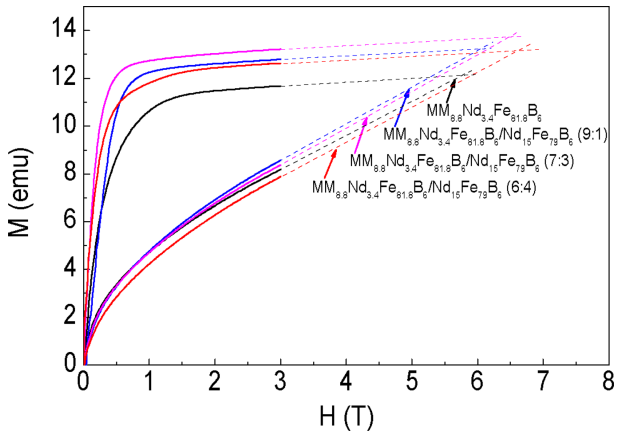

Fig. 6. (Color online) The magnetizing curves and their extended lines in the orientations of easy and hard magnetizing axes.

In the magnets with the mass ratio of 6:4, the degree of Nd atoms diffusing into (La,Ce)-rich main phase could be better owing to the optimization of Nd-rich main phase distribution, and so the nucleation field of reversed domain enhances in (La,Ce)-rich main phase, leading to the significant increase of coercivity. The inset of Fig. 5 shows that the activation size d_{active} reduces with the increase in the addition amount of $Nd_{15}Fe_{79}B_6$, This fact verifies the increase of the anisotropy at grain outer-layer, because the increase of anisotropy leads to the reduction of the domain wall size based on the formula of $\delta_m = \pi\sqrt{A/K}$ (A is the exchange coefficient and K is magnetocrystalline anisotropy) [28].

In the sintered magnets with dual-main-phase the magnetization reversal may not occur independently in (La,Ce)-rich main phase due to the exiting of high anisotropy phase of Nd-rich main phase. For check the magnetocrystalline anisotropy the magnetizing curve were recorded and extended to the intersection in the orientation of easy and hard magnetization axes, respectively, to estimate the anisotropy (shown in Fig. 6) [29], which are 5.8 T, 6.0 T, 6.5 T and 6.6 T, respectively for the mass ratios of 10:0, 9:1, 7:3, and 6:4. Due to the inhomogeneous microstructure the anisotropy value is a mean value in the sintered composite magnets. The increase ratio of coercivity is greater than that of magnetocrystalline anisotropy, implying that the coercivity enhancement does not entirely originate from the mean value of anisotropy. Both the diffusion of Nd into the grain outer-layer of La-Ce-rich main phase and the local regions of Nd-rich main phase should contribute to improve the coercivity. Optimizing the distribution of main phases and regulating the elemental diffusion are necessary to further

enhance magnetic properties in the sintered composite magnets.

4. Conclusions

In summary, the coercivity and phase distribution were investigated in the sintered composite magnets prepared by blending (MM,Nd)-Fe-B with Nd-Fe-B. The effect of enhancing the coercivity is weak in the magnets with the mass ratio 8:2 of (MM,Nd)-Fe-B and Nd-Fe-B. With the increase of Nd-Fe-B addition amount the size of reversed domain wall is reduced in the magnetization reversal, implying an increase of anisotropy at the grain outer-layer in (La,Ce)-rich main phase. For the mass ratio of 6:4 the coercivity increases significantly, and the coercive field of 7.70 kOe with the energy product of 33.67 MGOe was acquired in the magnet of $MM_{8.8}Nd_{3.4}Fe_{81.8}B_6/Nd_{15}Fe_{79}B_6$. Most grains of (La,Ce) main phase are nearly surrounded by the Nd-rich main phase and the intergranular phase, which could promote the diffusion of Nd into (MM,Nd)-Fe-B alloy. Both the optimization of Nd-rich main phase distribution and Nd substituting for La-Ce are responsible for the significant increase of coercivity in the sintered composite magnets.

Acknowledgements

The present work was supported by the National Natural Science Foundation of China (Grant No. 51861030), and the Inner Mongolia Autonomous Region Natural Science Foundation (Grant Nos. 2019MS01002 and 2020MS01007).

References

[1] J. Bauer, M. Seeger, A. Zern, and H. Kronmüller, J. Appl. Phys. **80**, 1667 (1996).
[2] H. L. Li, X. H. Li, D. F. Guo, L. Lou, W. Li, and X. Y. Zhang, Nano Lett. **16**, 5631 (2016).
[3] X. H. Li, L. Lou, W. P. Song, Q. Zhang, G. W. Huang, Y. X. Hua, H. T. Zhang, J. W. Xiao, B. Wen, and X. Y. Zhang, Nano Lett. **17**, 2985 (2017).
[4] A. H. Li, L. L. Xi, H. B. Feng, N. Zou, M. Tan, M. G. Zhu, and W. Li, J. Iron. Steel. Res. Int. **27**, 1 (2020).
[5] X. H. Li, L. Lou, W. P. Song, G. W. Huang, F. C. Hou, Q. Zhang, H. T. Zhang, J. W. Xiao, B. Wen, and X. Y. Zhang, Adv. Mater. **29**, 1606430 (2017).
[6] J. Yamasaki, H. Soeda, M. Yanagida, K. Mohri, N. Teshima, O. Kohmoto, T. Yoneyama, and N. Yamaguchi, IEEE Trans. Magn. **22**, 763 (1986).
[7] Z. R. Zhao, X. Wang, X. F. Zhang, Q. Ma, Y. L. Liu, Y. F. Li, F. Liu, and G. F. Wang, J. Magn. **22**, 60 (2017).
[8] R. S. Lai, R. J. Chen, W. Z. Yin, X. Tang, Z. X. Wang, C. X. Jin, D. Lee, and A. R. Yan, J. Alloys Comp. **724**, 275 (2017).
[9] Y. L. Liu, Q. Ma, X. Wang, J. J. Zhou, T. Y. Zhao, F. X. Hu, J. R. Sun, and B. G. Shen, Chin. Phys. B **29**, 107504 (2020).
[10] K. Y. Ko, S. Yoon, and J. G. Booth, J. Magn. Magn. Mater. **176**, 313 (1997).
[11] Z. B. Li, J. Z. Li, Z. Y. Xu, Y. F Li, and X. F. Zhang, J. Magnetics. **25**, 43 (2020).
[12] R. P. Chaudhary, K. H. Gandha, F. Q. Meng, E. Simsek, I. C. Nlebedim, O. Rios, M. J. Kramer, and R. T. Ott, Acs. Comb. Sci. **22**, 248 (2020).
[13] L. L. Zhang, M. G. Zhu, L. W. Song, T. Liu, Y. K. Fang, Y. J. Guo, W. Sun, and W. Li, J. Magn. Magn. Mater. **490**, 165414 (2019).
[14] J. Y. Jin, M. Yan, T. Y. Ma, W. Li, Y. S. Liu, Z. H. Zhang, and S. Fu, Mater. Design. **186**, 108308 (2020).
[15] D. Liu, T. Y. Ma, L. C. Wang, Y. L. Liu, T. Y. Zhao, F. X. Hu, J. R. Sun, and B. G. Shen, J. Phys. D: Appl. Phys. **52**, 135002 (2019).
[16] M. Sagawa, S. Fujimura, H. Yamamoto, Y. Matsuura, and K. Hiraga, IEEE Trans. Magn. **20**, 1584 (1984).
[17] C. J. Yan, S. Guo, R. J. Chen, D. Lee, and A. R. Yan, Chin. Phys. B **23**, 107501 (2014).
[18] X. Q. Yu, M. G. Zhu, W. Q. Liu, W. Li, Y. C. Sun, X. N. Shi, and M. Yue, J. Magn. Magn. Mater. **449**, 390 (2018).
[19] G. W. Huang, X. H. Li, L. Lou, Y. X. Hua, G. J. Zhu, M .Li, H. T. Zhang, J. W. Xiao, B. Wen, M. Yue, and X. Y. Zhang, Small. **14**, 1800619 (2018).
[20] G. C. Hadjipanayis, Y. F. Tao, and K. Gudimetta, Appl. Phys. Lett. **47**, (1985) 757.
[21] M. Yan, J. Y. Jin, and T. Y. Ma, Chin. Phys. B **28**, 077507 (2019).
[22] Q. Z. Jiang, W. K. Lei, L. K. He, Q. W. Zeng, S. U. Rehman, L. L. Zhang, R. H. Liu, S. C. Ma, and Z. C. Zhong, J. Alloys Comp. **775**, 449 (2019).
[23] W. Li, L. Z. Zhao, and Z. W. Liu, J. Magn. Magn. Mater. **476**, 302 (2019).
[24] H. Kronmüller, and M. Fahnle, Micromagnetism and the Microstructure of Ferromagnetic Solids. Cambridge University Press. 420 (2003).
[25] Z. B. Li, B. G. Shen, M. Zhang, Y. Zhang, F. X. Hu, and J. R. Sun, Appl. Phys. Lett. **106**, 042403 (2015).
[26] E. P. Wohlfarth, J. Phys. F: Met. Phys. **14**, L155 (1984).
[27] Z. B. Li, B. G. Shen, E .Niu, R. M. Liu, M. Zhang, and J. R. Sun, Chin. Phys. B **22**, 117503 (2013).
[28] E. F. Kneller and R. Hawig, IEEE Trans. Magn. **27**, 3588 (1991).
[29] Z. Li, W. Q. Liu, S. S. Zha, Y. Q. Li, Y. Q. Wang, D. T. Zhang, M. Yue, J. X. Zhang, and X. L. Huang, J. Magn. Magn. Mater. **393**, 551 (2015).